The Space and Time Features of Global SST Anomalies Studied by Complex Principal Component Analysis

Silvia Alessio, Arnaldo Longhetto

Dipartimento di Fisica Generale, Universita di Torino, Turin, Italy

and Istituto di Cosmogeofisica del CNR, Turin, Italy;

ICSC-World Laboratory, Lausanne, Switzerland,

Luo Meixia (骆美霞)

Institute of Atmospheric Physics, Chinese Academy of Sciences, Beijing 100029,

and International Centre of Theoretical Physics, Trieste, Italy

(Received August 23, 1996; revised May 21, 1998)

ABSTRACT

In this paper, the variability characteristics of the global field of sea surface temperature (SST) anomaly are studied by complex principal component (c.p.c.) analysis, whose results are also compared with those of real p.c. analysis. The data consist of 40 years of global SST monthly averages over latitudes from 42.5°S to 67.5°N. In the spatial domain, it is found that the distribution of the first complex loading amplitude is characterized by three areas of large values: the first one in the eastern and central equatorial Pacific Ocean, the second one in the northern tropical Indian Ocean and South China Sea, the third one in the northern Pacific Ocean. As it will be explained, this pattern may be considered as representative of El Niño mode. The first complex loading phase pattern shows a stationary wave in the Pacific (also revealed by real p.c. analysis) superimposed to an oscillating disturbance, propagating from the Pacific to Indian or the opposite way. A subsequent correlation analysis among different spatial points allows revealing disturbances actually propagating westward from the Pacific to the Indian Ocean, which could therefore represent reflected Rossby waves, i.e. the west phase of the signals that propagate disturbances of thermal structure in the tropical Pacific Ocean. In the time domain, a relation between the trend of the first complex principal component and the ENSO cycle is also established.

Key words: Global sea surface temperature anomalies, ENSO, Complex principal component analysis, Travelling disturbances

1. Introduction

Principal component analysis has been widely used to study the temporal and spatial behaviour of atmospheric and oceanic fields. A few years ago Barnett (1983) and Horel (1984) applied to geophysical data sets a complex principal component (c.p.c. hereafter) analysis method in the time domain, which is an extension of the real principal component (henceforth r.p.c.) method. Using both methods, Fu et al. (1988) analyzed the equatorial Pacific Ocean data of sea surface temperature (SST) from 30°S to 30°N; Longhetto et al. (1993) analyzed monthly averages of SST data of the Pacific Ocean, from 10°S to 50°N and from 120°E to 80°W, from January 1949 to December 1987.

In the present paper, c.p.c. and r.p.c. analyses, associated with the analysis of point correlation features of original and c.p.c.-reconstructed data, are used to study spatial and

temporal characteristics of global SST anomalies on a decadal scale. The aim of the study was to reveal possible travelling waves in the anomaly field, that may be responsible for climatic teleconnections. Particular attention was paid to detecting features related to the occurrence of El Niño events.

2. Data set

The data set used in this paper consists of monthly averages of global SST over 40 years.

The original sample was properly homogenized, in order to minimize the differences in precision and sensitivity of the instruments employed throughout the years, and finally was interpolated to a regular spatial grid, whose mesh is 5 degrees in latitude by 5 degrees in longitude, extending from 42.5°S to 67.5°N. The total number of grid points (also "stations" hereafter) is $N = 1193$, while the total number of time steps in each SST series is $M = 480$ (from October 1948 to September 1988). The data were taken from U. K. Met. Office.

The SST data were then converted into standardized anomalies (SSTA) before use. This was obtained by subtracting to each monthly datum at each station the average SST over 40 years, computed at that station for that month of the year, and then dividing the result by the corresponding standard deviation. N time series with zero mean and unit standard deviation were thus obtained. In the discussion that follows, we shall refer to these standardized anomalies as to "original data".

3. The c.p.c. method

The c.p.c. method, which is an extension of the r.p.c. method to the complex field, was adapted by Barnett (1983) and Horel (1984) to describing space and time behaviour of geophysical data sets. The advantage of the extension lies in the fact that c.p.c is able to reveal also travelling disturbances of the field, rather than just standing oscillations (as r.p.c. does).

Let $u(t_k, x_j)$ represent a scalar field as a function of time t and space x. For the sake of simplicity, this field will be supposed centered (that is, with zero mean). Time is known at discrete instants $(t_k, k = 1, M)$; space too corresponds to discrete positions $(x_j, j = 1, N)$. A new "augmented" complex field U_{kj} is constructed by

$$U_{kj} = u_{kj} + i\hat{u}_{kj}$$

with $i = \sqrt{-1}$. The real part u_{kj} represents the original scalar field, while the imaginary part $\hat{u}_{kj}$ is an element of the Hilbert transform of the time series represented by $u_{kj}, k = 1, M$. In the present work, the Hilbert transform in practice was obtained (1984) via FFT. In order to avoid end effects, the transformed series were truncated, by rejecting 6% of the samples at the head and tail of each series. Therefore the augmented field is known at M' discrete times only, with $M' = 422$.

The correlation matrix r of the complex field U_{kj} is a Hermitian matrix, whose elements are given by

$$r_{jl} = \frac{1}{M'} \sum_{k=1}^{M'} U_{kj}^* U_{kl},$$

where the asterisk denotes complex conjugation. This Hermitian matrix has real eigenvalues λ_l and a set of complex orthonormal eigenvectors V_{jl} $(j, l = 1, N; l$ indicates mode, j spatial

position as before).

Each mode explains a certain percentage of the total variance of the augmented input field; modes are ordered according to decreasing percentage of explained variance (that is, according to decreasing eigenvalue). The interest of the method lies in the fact that normally the curve of explained variance percentage as a function of mode falls off rapidly enough to allow retaining only a few modes, explaining individually and / or cumulatively a significant part of the total variance, thus simplifying the analysis.

The c.p.c.s are new independent time series given by

$$T_{kl} = \sum_{j=1}^{N} U_{kj} V_{jl} \qquad (k = 1, M');$$

the elements of the l–th complex loading vector are found by

$$L_{jl} = V_{jl} \sqrt{\lambda_l},$$

while the complex correlation R between the input augmented complex series at the j–th grid point and the l–th c.p.c. series is defined as

$$R_{jl} = V_{jl} \frac{\sqrt{\lambda_l}}{S_j},$$

where S_j denotes the standard deviation of the j–th input augmented series (U_{kj}, $k = 1, M'$).

In the case of the present study, input augmented series were standardized, so that $S_j = 1$; therefore loading L_{jl} and correlation R_{jl} coincide. Moreover, the spatial pattern of a given complex eigenvector and that of the corresponding complex loading are obviously the same, since an element of the loading matrix is obtained by the analogous eigenvector element by merely multiplying by the constant $\sqrt{\lambda_l}$.

It is useful (Barnett, 1983) to separate complex quantities relative to the l–th mode, such as T_{kl}, with $k = 1, M'$, and V_{jl}, with $j = 1, N$, into amplitude and phase parts, thus getting four measures that define possible moving features in the field u_{kj}. The first two of these measures (Temporal Amplitude Function, henceforth indicated by the acronym TAF, and Temporal Phase Function, henceforth TPF) are defined in the time domain and are related each to a column of T matrix, while the other two are spatial quantites related each to a column of V matrix (SAF, Spatial Amplitude Function, and SPF, Spatial Phase Function; SPF, as well as TPF, is known only to within an additive constant, a fact that in the real case corresponds to p.c.s and eigenvectors defined only to within a sign change). In the present paper, however, rather than in terms of SAF, the spatial amplitude pattern will be described in terms of AMC (Amplitude of Correlation), that is, directly in terms of the amplitude of the complex correlation matrix R.

In agreement with this choice, the spatial pattern of a real eigenmode will be described in terms of correlation between the original time series at a given station and the r.p.c. series for that mode (due to the standardization applied, this correlation coincides with the corresponding real loading). This quantity will be referred to as COR and may obviously be of both signs (while AMC is the amplitude of a complex quantity and therefore is always positive). R.p.c. time series will be indicated by the acronym PCO.

The acronyms introduced here will be used throughout the paper and, when referring to a particular r.p.c. or c.p.c mode, they will be followed by the corresponding order number: e.g., AMC1 = "AMC for mode n.1".

The c.p.c. method (as well as the r.p.c. one) also allows approximate (that is, simplified, smoothed) reconstruction of the input field on the basis of a certain number $N' \leqslant N$ of eigenmodes. The reconstructed field u'_{kj} is given by

$$u'_{kj} = Re(\sum_{l=1}^{N'} T_{kl} V^*_{jl}),$$

where N' stands for the number of c.p.c'.s selected for the reconstruction, under some criterion based upon the percentage of explained variance.

4. Results of c.p.c. and r.p.c. analyses

The first complex mode explains 9.1% of the total variance of the SSTA field. The second mode explains 5.3%, the third 3.4%, the fourth 3.1% etc.; the first three c.p.c. modes cumulatively explain about 18% of the total variance. If one considers the first six modes, this figure becomes about 26% and attains about 37% with the first twelve modes; however, it is not useful to select an elevated number of modes, because from the fourth one on the percentage of variance explained individually becomes very low (less than 3%) and probably merely reflects noise in the signal.

The first real mode explains 8.8% of the total variance of the SSTA field. The second mode explains 4%, the third 2.8%, the fourth 2.6%, the fifth 2.4% etc..

In the following subsections, the features of the first complex mode will be extensively described and compared with those of the first real mode. A brief account of interesting features concerning the second and third complex modes will also be given.

4.1 *Space features*

4.1.1 *Amplitude of the first complex loading (AMC1)*

Being the amplitude of a complex number, AMC is always positive and as a correlation coefficient, it may vary between 0 and 1. AMC1 corresponds, as already said, to 9.1% of the total variance.

In Fig. 1, the contour map of AMC1 is shown. Fig. 2 shows the corresponding detailed space distribution of the values of AMC1 exceeding a threshold value 0.3: this value was chosen conservatively after carrying out a T test for statistical correlation coefficients, with $\alpha = 0.01$, which showed that for a sample size of 480, the critical correlation coefficient value is 0.23. In the figure, the values of AMC1 appear multiplied by 100.

In the same figure, nine of "zones of interest" (including relatively high values of AMC1), that will be of help in the following discussion, are also indicated. The criterion by which these zones were precisely defined is described in detail in Section 5, concerning SSTA point correlation analysis method. Fig. 3 shows instead the positions at which the highest values of AMC1 (>0.6) are found.

As it can be seen from Fig. 2, the interest in this first mode is centered on the Pacific and, in general, on the oceans in the intertropical belt, in the sense that in these regions AMC1 is greater than the threshold value 0.3.

Looking at Fig. 1, three areas of elevated amplitude (>0.4) are recognizable: the first one occurs in the eastern and central equatorial Pacific (ECEPO hereafter); the maximum value is 0.76 and is located at [112.5°W, 7.5°S]. This wide area extends across the Equator from about 20°S to 10°N and from about 165°E to the coast of South America.

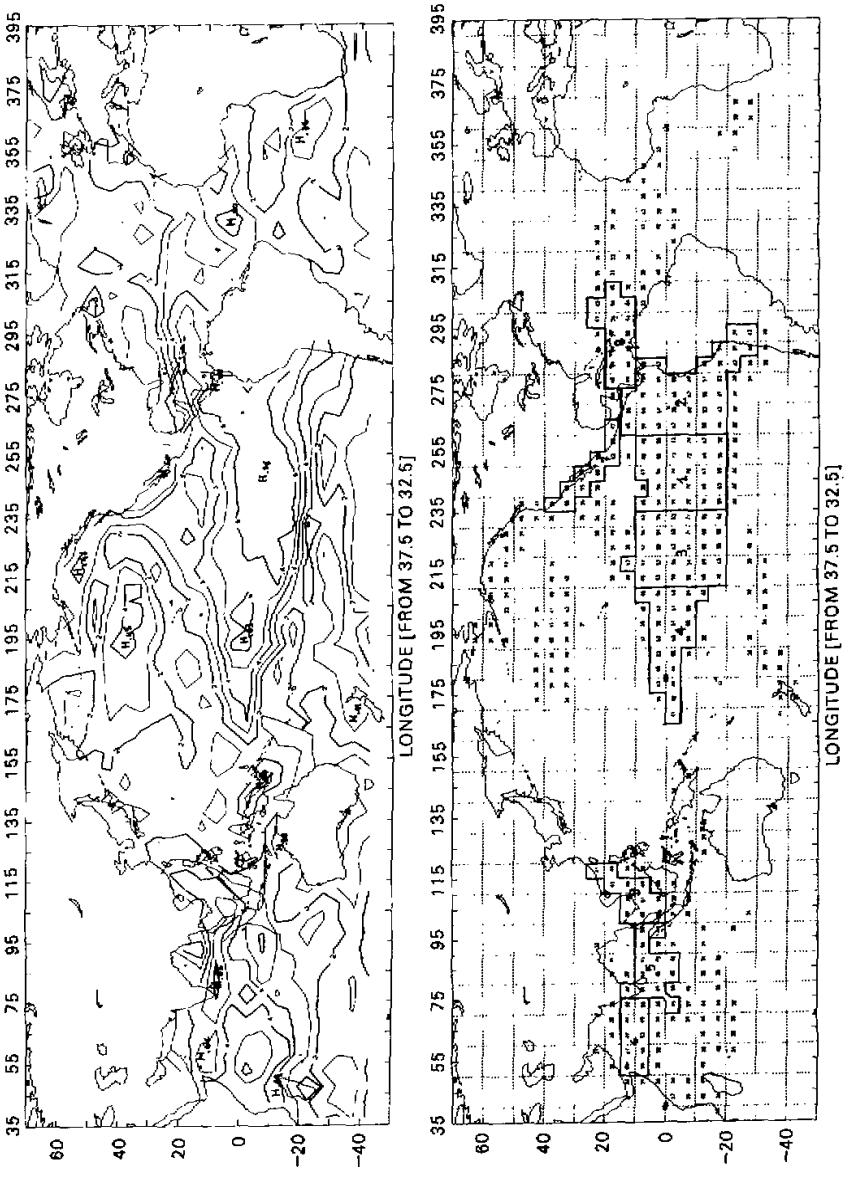

Fig. 1. Spatial pattern of the first complex loading amplitude (AMC1), shown by contour lines.

Fig. 2. Values of the first complex loading amplitude (AMC1) exceeding the threshold 0.3, multiplied by 100. The areas numbered from 1 to 9 represent the "zones" quoted in Sections 4 and 6 and described in Section 5.

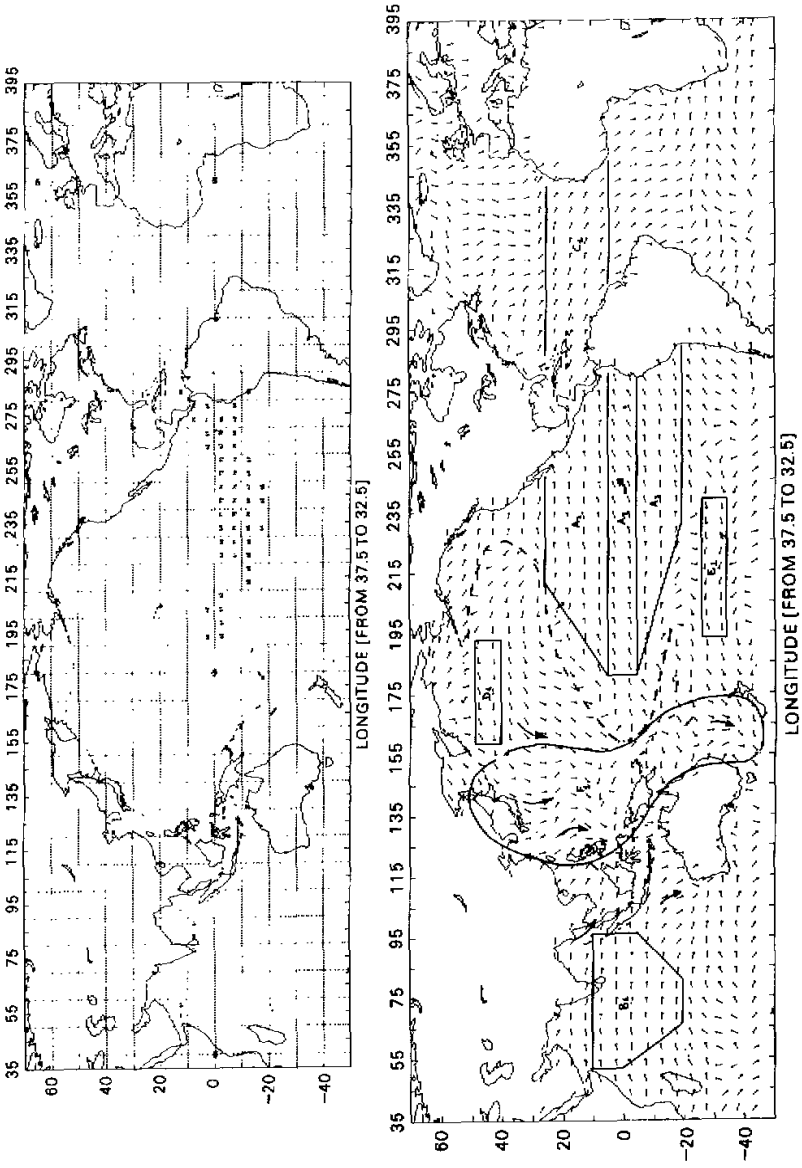

Fig. 3. Values of the first complex loading amplitude (AMC1) exceeding the threshold 0.6, multiplied by 100.

Fig. 4. Spatial pattern of the first complex loading phase (SPF1). Each phase is represented as a vector departing from the grid point it belongs to. Areas labelled as A_1, B_1, C_1, D_1 and E_1 represents zones of uniform phase; area F_1 represents a zone of phase change and corresponds to low AMC1 values (see text). The curved arrows in the figure are meant to suggest vector rotation. The dashed S-shaped curve is a nodal line of a stationary wave, present in the Pacific Ocean.

The second area extends over the northern tropical Indian Ocean and the South China Sea (NTIO, SCS hereafter, respectively); the maximum value is 0.63 and is located at [82.5°E, 7.5°N]. This area spans from about 50°E to 120°E across the 10°N parallel.

Fig. 3 in fact reveals that the highest values, i.e. larger than 0.6, are spread over south tropical regions of the eastern Pacific Ocean (south-tropical portion of zones n.1, n.2 and n.3 in Fig. 2, with the above quoted absolute maximum of 0.76 inside zone n.1), over scattered points of the equatorial central Pacific Ocean (zone n.4 of Fig. 2) and in a few locations of the NTIO (where the second maximum of 0.63 occurs, inside zone n.5). A few values larger than, or equal to, 0.60 are also found in the northern equatorial belt of zone n.2. Slightly lower values of AMC1 (from 0.50 to 0.60), appearing in Fig. 2, stretch over the southern border of zone n.2 and can be also found in regions occupying the northern boundary of the previously mentioned zones n.1, 3 and 4, up to about 10°N, and in a few locations of the SSC (inside zone n.9).

Lower values of AMC1 (from 0.30 to 0.50) can be found in the central equatorial Pacific Ocean, west of the date line, in the warm-pool region; in the north-east Pacific Ocean and in the north-tropical Atlantic Ocean, up to about 20°N; in the south tropical Indian Ocean and in the south Pacific Ocean.

The third area of elevated AMC1 (in order of decreasing value of the AMC1 relative maximum included inside it) appears in the northern Pacific Ocean (NPO): the maximum amplitude is 0.47 at [142.5°W, 52.5°N]. Less extended highs also appear in the southern Pacific Ocean ([165.5°E, 37.5°S]; value 0.41), in the central Atlantic Ocean ([27.5°W, 2.5°N]; value 0.50) and in the western Indian Ocean, north of the coast of Madagascar ([47.5°E,12.5°S]; value 0.49).

The Indian Ocean is divided from the Pacific by a belt of very low values (<0.3 and therefore not present in Fig. 2), extending from about 125°E to 165°E.

The fact that in the latitude belt 0°–10°N, which is the region swept by the seasonal movements of the ITCZ, AMC1 attains larger values over the central and eastern north-equatorial Pacific Ocean (up to 10°N) than over the north-equatorial Atlantic Ocean (in the Atlantic Ocean the highest values are found in the belt from 10° to 20°N), is a first evidence of an El Niño signature, corresponding to its inhibiting action on the northward movement of the ITCZ in the Pacific Ocean early in autumn.

As the following Fig. 4 (showing the distribution of spatial phases for the eigenmode n.1, discussed later on in Subsection 4.1.2) shows, the regions of the Pacific–Indian Ocean system, belonging entirely or partially to the zones numbered as 1, 2, 3, 4 and 5, 6 in Fig. 2, all exhibit the same phase, which keeps practically constant all through them (that are labelled as regions A_1 and B_1 in Fig. 4). However, the wide region made up of zones n.1, 2, 3 and 4 of Fig. 2 and labelled as zone A_1 in Fig. 4 contains an inner equatorial belt, where the phase of the first spatial mode shows a progressive counterclockwise turning, when moving from the date-line to the eastern boundary of the oceanic basin, which could mark a propagating disturbance along the W–E direction.

Zhang et al. (1997) analyzed the interannual and lower frequency variations of SST through the entire Pacific Ocean, by evaluating the space distribution of the leading r.p.c.s both with a high-pass filter and with a low-pass filter.

They found a pattern of the higher-frequency SST variability, which represents the El Niño – Southern Oscillation (ENSO) phenomenon closely confined to the equator, and a pattern of the lower-frequency variability, which is much less spatially confined to the tropics and shows a decadal mode, providing a different background state for those ENSO variations

that are more equatorially confined.

If we look at Fig. 3 we can see that the largest AMC1 values (>0.7) in the south ECEPO are actually confined to the equator, while AMC1 values >0.3 (Fig. 2) are more spread and conform more closely to the low-frequency variability pattern found by Zhang et al. (1997).

It may be interesting to notice that if one repeats the analysis selecting only those time steps in the N time series that correspond to El Niño events (133 time steps), one gets a c.p.c. n.1 (explaining about 10% of the data variance) whose overall AMC1 characteristics (not shown) coincide with those described above, in particular for what concerns the highs in NTIO and ECEPO.

4.1.2 *Phase of the first complex loading (SPF1)*

SPF is an important tool for identifying travelling structures. As already mentioned in Subsection 4.1.1, however, this quantity is known only to within an additive constant, so that only phase differences between the various spatial positions matter; therefore only the propagation direction of waves can be identified (and not the way the oscillation travels). Spatial phases will be represented as vectors departing from the grid point they belong to.

A general characteristic of the phase spatial maps, that shall be described here and later, is that in areas in which the corresponding amplitude is low, the phase becomes (obviously) irregular and "noisy". Therefore in the discussion we shall focus our attention on areas in which the corresponding amplitude is relatively large; in these areas we shall sometimes find constant phases or, instead, phases that seem to vary regularly, thus suggesting the idea of a propagating wave. Of course, the two aspects may be superimposed to one another.

Fig. 4 shows SPF1. In the same figure, areas with particular characteristics, discussed ahead in the text, are also marked. Two large homogeneous areas are present, one including ECEPO (region A_1) and the other one including NTIO (region B_1). These two regions, that correspond to elevated AMC1 (see previous discussion in Subsection 4.1.1), have nearly constant and equal phases; however, as already said in Subsection 4.1.1, the wide region A_1 contains an inner equatorial belt, where the phase of the first spatial mode shows a progressive counterclockwise turning, when moving from the date-line to the eastern boundary of the oceanic basin, which could mark a disturbance propagating along the W-E direction.

Moreover, in the equatorial belt, even in the Atlantic the phase is nearly the same as in the Pacific (region C_1); only the belt F_1, corresponding to very low AMC1 scores (see previous subsection) interrupts this continuity. In Pacific regions D_1 and E_1 the phase is also nearly homogeneous and opposite to that of regions A_1 and B_1, a fact that suggests the existence of a stationary wave, typical of the warm and cold phases of the SO, with a nodal line along the reversed-S shaped dashed curve shown in the figure. Here and there along the curve, it is possible to see the vector that undergoes a phase reversal from one grid point to the neighbouring one.

At the edges of the area F_1 (as well as inside it) there is some evidence of propagating disturbances, travelling from Pacific to Indian or the opposite way (the curved arrows in the figure merely try to suggest the rotation of phase vectors).

Another region of possible propagation is present in the southern Indian Ocean but corresponds to lesser AMC1 scores; the same is true for two more regions of phase homogeneity in the Atlantic.

The phase pattern of Fig. 4, and particularly its area F_1, suggests that, superimposed on a strong ENSO signal, some features of the seasonal cycle in the Pacific, Indian and Atlantic

Ocean still appear. The area F_1, stretching south-eastward across the southwestern tropical Pacific Ocean and separating the central tropical Pacific Ocean from the NTIO, is actually the region over which the seasonal movements of the South Pacific Convergence Zone (SPCZ) occur.

4.1.3 *First real loading (COR1)*

Fig. 5 shows, for comparison with those of AMC1 and SPF1, the spatial distribution of COR1 (absolute values in the range [0.–1.]). As for AMC1, it may be said that this first real mode mainly represents the Pacific Ocean and, in general, all the intertropical belt (this in fact is the area over which COR1 assumes absolute values greater than the threshold 0.3).

In the central Pacific Ocean, the pattern tipically shows regions of positive and negative COR1 alternating along parallels. Low (negative) Pacific centers are: −0.76 at [122.5°W, 7.5°S] (ECEPO; this center practically coincides with the absolute AMC1 maximum); −0.63 at [167.5°W, 2.5°S] and −0.56 at [112.5°W, 27.5°N] (along a belt that from the Equator stretches northward up to the Pacific coast of Mexico); −0.43 at [142.5°W, 52.5°N], in the north-eastern Pacific Ocean. A high (positive) Pacific center (value 0.52) is located at [157.5°W, 32.5°N]; with weaker intensity, other highs are found in south Pacific.

Moving now to the Indian Ocean, the second strongest negative maximum of COR1 (after the one in ECEPO) is located in NTIO at [82.5°E, 7.5°N] and coincides with the second AMC1 maximum; the value is −0.73. Another low in NTIO occurs at [57.5°E, 12.5°S], with a value of −0.71; the whole belt connecting in NTIO these two peaks has very negative values. Moreover in the eastern Indian Ocean, north of the coast of Madagascar [47.5°E, 12.5°S], a low with −0.58 is found. It coincides with one of the AMC1 maxima.

Finally, low centers are found in the equatorial [32.5°W, 2.5°S] and tropical [7.5°E, 22.5°S] Atlantic Ocean too, with values of −0.47 and −0.46 respectively.

From Fig. 5 it may be seen that the SSTA in ECEPO is positively correlated with that in the Indian Ocean and in the SSC (as well as with central and southern Atlantic), while it is anti-correlated with the SSTA in the northern and southern Pacific Ocean, a fact that confirms what was said about the SPF1 pattern in Subsection 4.1.2. A curved (with reversed S-shape) line of null correlation is found in the Pacific; this supports the existence of a stationary wave, already suggested by SPF1 inspection.

4.1.4 *Second and third complex modes*

The AMC2 pattern is shown in Fig. 6; it concerns mainly the Atlantic Ocean and the NPO (latitudes greater than 40°N) and is responsible for 5.3% of the total variance. The largest amplitude area extends over the northern Atlantic Ocean; the maximum value is 0.65 at [27.5°W, 57.5°N]. A second, less extended peak occurs in the Southern Atlantic Ocean; the value is 0.51 at [32.5°W, 12.5°S]. There are other relative high centers in the NPO (0.48 at [47.5°N, 152.5°E] and 0.47 at [127.5°W, 52.5°N]; 0.40 at [172.5°W, 47.5°N]), in the SSC (0.41 at [122.5°E, 22.5°N]) and in the central equatorial Pacific (0.41 at [162.5°W, 2.5°N]).

Fig. 7 shows the pattern of SPF2. Regions of phase homogeneity are labelled (according to decreasing AMC2 values) A_2, B_2, C_2 in the Atlantic (with n. B_2 in opposition of phase to regions A_2 and C_2), D_2 , E_2 in the northern and central Pacific (same phase), F_2 in the southern Indian Ocean, G_2 in the South Pacific Ocean. Regions D_2 and E_2 are phase-opposite to region F_2. In the Atlantic, the picture suggests the presence of a stationary wave, with nodes around the parallels 0–10°N and 30°S, superimposed to travelling waves (see arrows indicating vector rotation): the quadrature phase shift between the Azores region and the area

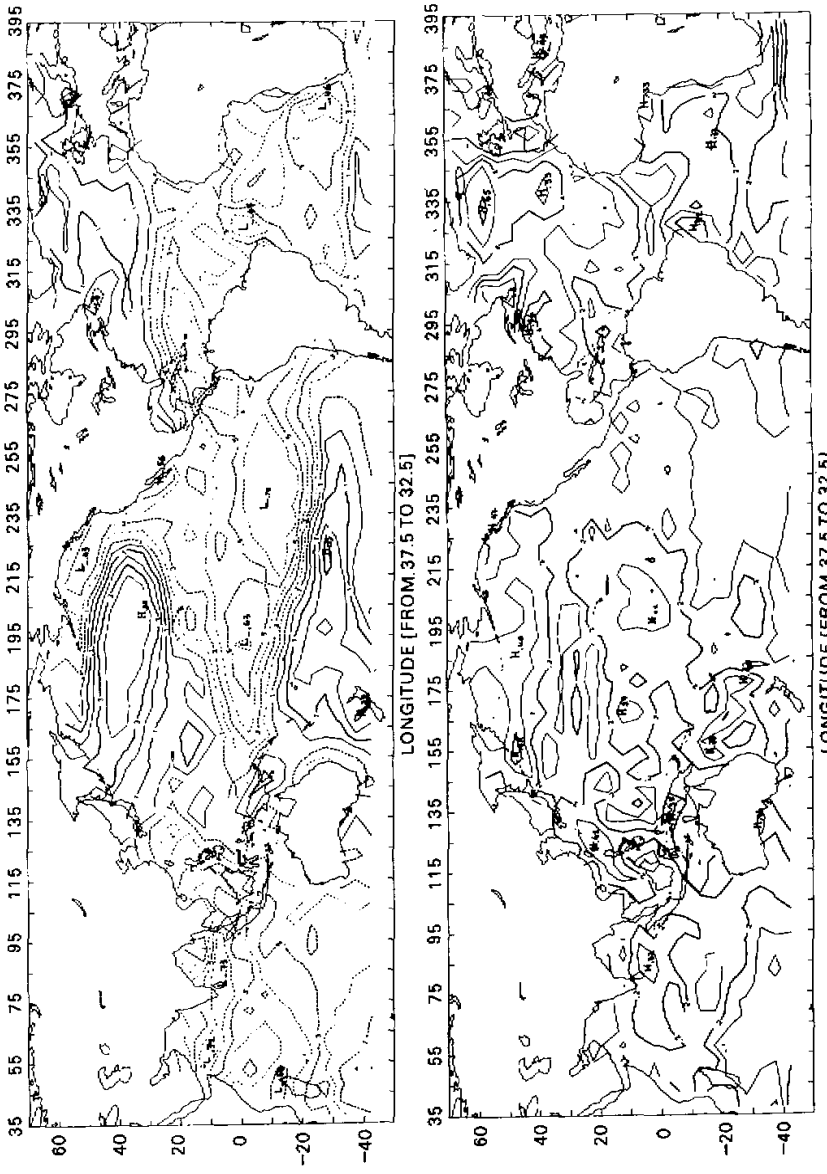

Fig. 5. Spatial pattern of the first real loading (COR1), shown by contour lines.

Fig. 6. Spatial pattern of the second complex loading amplitude (AMC2), shown by contour lines.

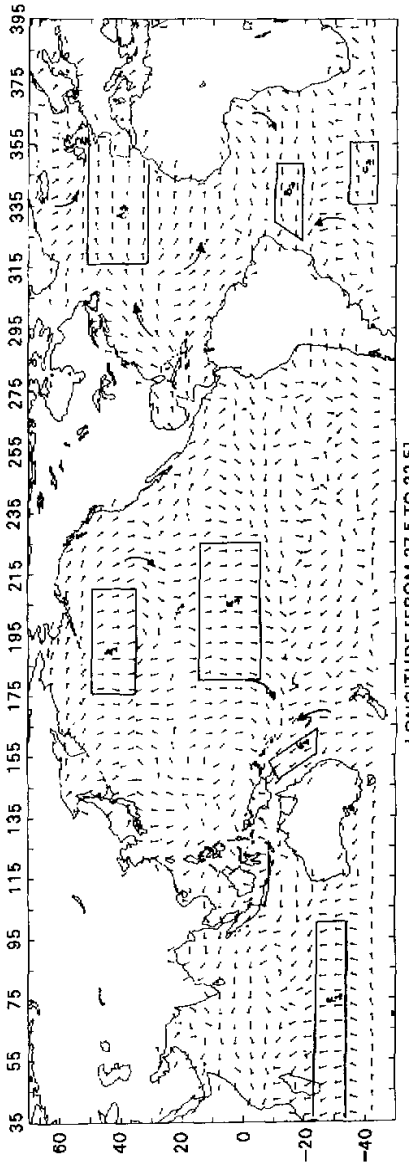

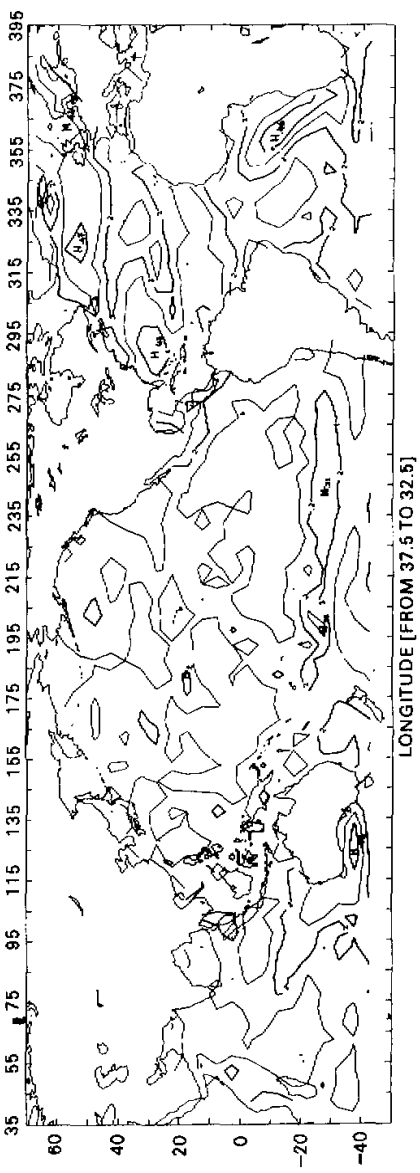

Fig. 7. Spatial pattern of the second complex loading phase (SPF2). Each phase is represented as a vector departing from the grid point to which it is relative. Areas labelled as A_2, B_2, C_2, D_2, E_2, F_2 and G_2 represent zones of uniform phase. The curved arrows in the figure are an attempt of suggesting vector rotation.

Fig. 8. Spatial pattern of the third complex loading amplitude (AMC3), shown by contour lines.

surrounding Iceland could be related to the North Atlantic Oscillation (NAO). Also in the Pacific there may be some propagation.

Fig. 8 shows the spatial distribution of AMC3 (3.4% of total variance). This mode is peculiar of the southern Australian Basin and of the Atlantic. The highest center (0.48) appears in the southern Indian Ocean, close to the South coast of Australia, at [122.5°E, 37.5°S]. Three centers of about the same magnitude are found in the Northern Atlantic Ocean (0.47 at [72.5°W, 27.5°N] and at [37.5°W, 52.5°N]) and in the south equatorial Atlantic Ocean (0.46 at [2.5°E, 12.5°S]).

In Fig. 9, SPF3 is shown. It suggests propagation in the southern Australian Basin and in the Atlantic. In particular, the tropical Atlantic Ocean, north of the equator, has a substantially constant phase (region A_3); smaller regions of phase homogeneity are also found towards Florida Coast (B_3) and in the southern Atlantic Ocean (C_3), while propagation may take place in the northern Atlantic and in the area of Angola Basin and Gulf of Guinea.

4.2 *Time features*

The first mode turned out to be, even in the time domain, the one best connected to all El Niño events that took place in 1951–1987.

4.2.1 *Amplitude of the first c.p.c. (TAF1)*

TAF1 is shown in Fig. 10. It presents intervals of relative maximum in the following years: 1953–1958, 1964, 1970–1974, 1976, 1979–1980 and 1983–1984. Table 1 shows, for comparison, the calendar of El Niño and La Niña events, according to an analysis made by Shi et al. (1990). It must be said, however, that there is not a general agreement about the dates of El Niño events of the last fifty years: the most widely accepted are perhaps 1953, 1957–1958, 1972–1973, 1976–1977, 1982–1983 and 1986–1988, in the time range covered by the present data set.

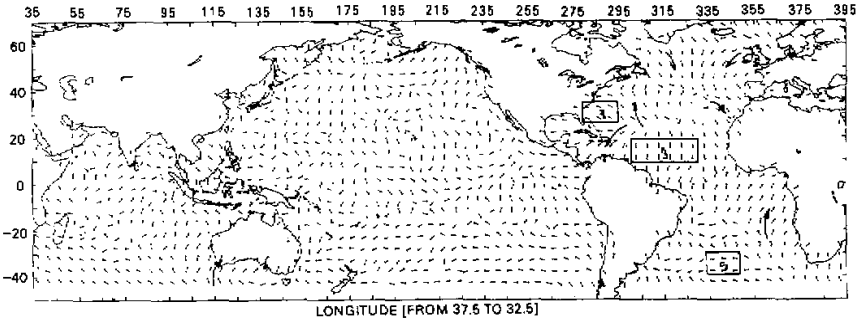

Fig. 9. Spatial pattern of the third complex loading phase (SPF3). At each grid point, the phase is represented as a vector departing from the grid point. Areas labelled as A_3, B_3 and C_3 represent zones of uniform phase. The curved arrows in the figure are there to suggest vector rotation.

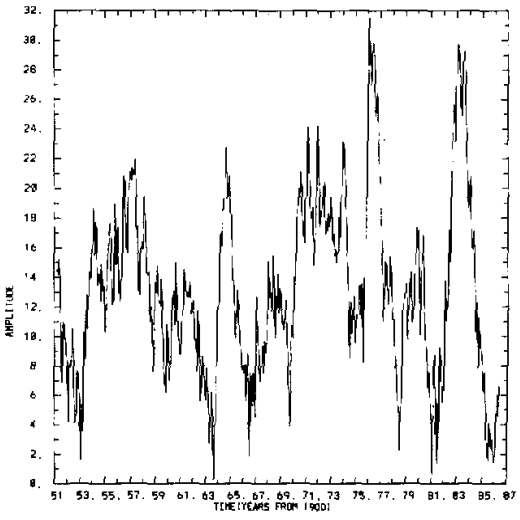

Fig. 10. Time plot of the first complex principal component amplitude (TAF1).

Looking at Fig. 10, it is interesting to notice that in the fifties, in which three warm events and one cold event took place, TAF1 remains high for a relatively long time; the same happens in 1970–1974, a period including an El Niño and two La Niña episodes. Other maxima correspond to El Niño 1976–1977, El Niño 79 and the strong El Niño of 1982–1983; also la Niña 1964–1965 is heavily felt. Minima correspond instead to El Niño events of 1963 and 1968–1970. All El Niño events universally accepted by all authors are on TAF1 maxima (except 1986–1988, which is lost due to time truncation in c.p.c. analysis). Moreover, TAF1 undergoes the greatest variations from the seventies on; in particular, there are two maxima of short duration but very intense in 1976 and in 1982–1983, in coincidence with El Niño events. Clarke et al.(1996), studying the trade winds system in the eastern Pacific, has found an overall weakening starting from the seventies. This weakening could be responsible for a greater impact of the ENSO phenomenon, which itself is characterized by a weakening of the trade winds in the eastern Pacific; an impact resulting in a TAF1 increase.

4.2.2 *Phase of the first c.p.c. (TPF1)*

The cycle of warm and cold events may be seen also in TPF1. Fig. 11 shows this quantity plotted against time. As already mentioned, TPF is known only to within an additive constant, so that only phase differences between the various time steps matter. In the work by Longhetto et al.(1993) (with data limited to the Pacific tropical area), an analogous plot shows that when the phase, starting from π, begins to decrease, a new El Niño event starts; crossing the zero line, the phase then becomes negative during La Niña events, eventually attains π again and a new cycle begins (the particular value π is obviously tied to the choice of the initial phase).

In the case of the present study this correspondence is somewhat less clear, due to the obvious influence of the other Oceans. In a p.c. study relative to the tropical Atlantic Ocean, Lough (1986) found elements supporting the hypothesis that to a positive anomaly in the

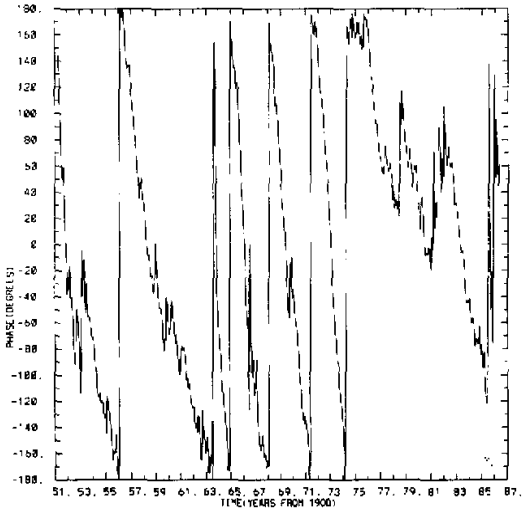

Fig. 11. Time plot of the first complex principal component phase (TPF1) in degrees.

Pacific (El Niño) may correspond a negative anomaly in the Atlantic, thus suggesting that an Atlantic El Niño may exist, even if of weaker intensity. For example, in 1982, according to Philander (1990), when an event ended in the Pacific, another one started in the Atlantic. Even if this may not be always the case, it is certain that ENSO influences the climate of the whole planet.

Comparing Fig. 11 with Table 1 it may however be seen that all El Niño events take place when the phase, after attaining a maximum, starts decreasing more or less regularly; cold events concentrate on negative ($-\pi$) peaks. The trend of TPF1 in the decreasing phase portion of each cycle is rather linear from $+\pi$ to $-\pi$, except than from 74 on (in particular around 1975, 1979 and 1982: the period in which TAF1 undergoes strong oscillations), when three positive peaks are found and $-\pi$ is no longer attained.

4.2.3 *First r.p.c. (PCO1)*

Also the first r.p.c. (Fig. 12) shows an alternate presence of positive and negative peaks; the negative peaks seem to be connected to El Niño events (except 1976–1977, which is not universally considered as an El Niño year), while the positive ones correspond to cold events (compare with El Niño and La Niña chronology, shown in Table 1). However, while the correspondence between relative minima and El Niño events is quite precise, cold events correspond to a maximum in a less strict sense.

This fairly good correspondence, that could be surprising when considering that the set of data includes all oceans, confirms (see COR1 discussion) that also the fist real mode, as the first complex one, is essentially an El Niño mode and is mainly under the influence of the Pacific events.

4.2.4 *Second and third complex modes*

TAF2 (not shown) has a nearly constant average value, with the two highest peaks

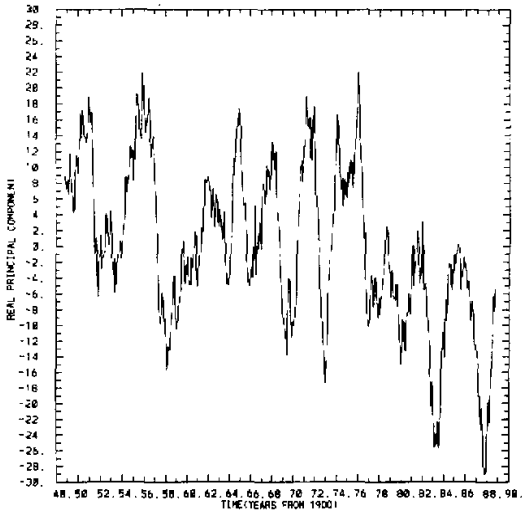

Fig. 12. Time plot of the first real principal component (PCO1).

Table 1. Time series of El Niño and La Niña events from 1949 to 1988

El Niño event		La Niña event	
Date	Duration (months)	Date	Duration (months)
June 1951 – February 1952	9	September 1949 – November 1950	15
April 1953 – November 1953	8	April 1954 – February 1956	23
April 1957 – July 1953	16	May 1964 – January 1965	9
July 1963 – January 1964	7	July 1967 – June 1968	12
May 1965 – March 1966	11	June 1970 – December 1971	19
November 1968 – January 1970	15	June 1973 – April 1974	11
April 1972 – February 1973	11	May 1975 – February 1976	10
June 1976 – March 1977	10	October 1984 – September 1985	12
September 1979 – June 1980	10	June 1988 – March 1989	10
May 1982 – October 1983	18		
September 1986 – February 1988	18		

corresponding to the terminal phase of La Niña 1954–1956 and to El Niño 1972–1973.

TAF3 (not shown) is characterized by the absence of outstanding peaks and by an average value that seem to present a quasi-sinusoidal oscillation, with the positive half-wave culminating at the beginning of the sixties and the negative one culminating around 1979; therefore in the seventies the average TAF3 is slightly lower than in the previous years (when TAF1, on the contrary, presents the highest peaks: on average the events of the last decades seem to be best represented by the first mode, while the third mode plays a slightly more important rôle in the fifties and sixties).

In summary, the second and third modes do not seem to express globally the El Niño

phenomenon, but rather seem to be influenced by some particular events.

5. Correlation analysis method

Correlation analysis in the present paper was employed as a tool for casting light upon certain results of c.p.c. analysis, concerning SPF1.

As said above, a c.p.c. mode may contain travelling waves, whose propagation may be detected in the phase spatial pattern SPF associated to that mode. However, this method allows recognizing the direction along which the wave propagates, but not the way it travels. For example, we have seen that the SPF1 pattern indicates the presence of waves travelling almost zonally, from the Pacific to Indian Ocean or vice-versa; but c.p.c. analysis does not tell us if the propagation is toward east or toward west. The way the disturbance propagates is obviously of fundamental importance and especially in ENSO phenomena it may help discriminating among Ekman drift, Kelvin waves, Rossby waves and other types of thermal re-adjustments or disequilibria (lacks of balance) due to dynamical forcings.

In this paper, an attempt was made to overcome this problem, by going back, after c.p.c. analysis, to the study of correlation functions $C(\tau)$ (where τ indicates temporal lag) between different grid points (or stations). The procedure that was followed will now be described.

At first, a restricted number of grid points, corresponding to relative maxima in the AMC1 spatial pattern, were correlated, at various lags, with all other grid points. Recall that these centers of elevated AMC1 characterize spatial positions at which the first c.p.c. has a higher statistical weight in the development of the original field on the basis of the eigenvectors of the spatial covariance matrix at lag $\tau = 0$ of the same field. They were therefore chosen as base stations for studying the spatial pattern of the correlation between the time series of SSTA at the base itself and the time series in all other grid points, for various values of τ, so as to be able to recognize the lead or lag with which a certain signal appears in these stations, with respect to the base. The value of correlation that is obtained, for a particular pair of points,① by coupling the series j at time t with the series j' at time $t+\tau$, has been compared with the other value of correlation that is obtained by coupling, on the contrary, SSTA(j,t) with SSTA($j',t-\tau$). From this comparison, one should expect to be able to reveal if a disturbance has travelled from point j to point j', or vice-versa. However, the elevated noise background characterizing this kind of data would not allow drawing sound conclusions about lead-lag relations between single spatial points; therefore, a more averaged-out comparison among smoothed correlations was preferred.

The points surrounding local relative maxima of AMC1 and characterized by "elevated" AMC1 were assigned each to a "zone". The zones are nine and are shown in Fig. 2. In some cases (see later), a zone too much extended in longitude was divided into smaller parts: being interested in evidencing structures propagating nearly zonally across the ocean, it was natural to separate group of stations progressively interested by the propagation of possible waves, especially in the intertropical belt. For each zone and for each lag, the average and extremal (positive or negative) correlation with the base, found inside the zone, were computed; these values were then plotted as function of lag, zone by zone. The information about possible lead-lag relations in the data was sought in the shape, lag extent and symmetry characteristics of these curves.

---

①This pair is formed by the base j and the grid point j': e.g. two points aligned along a direction of interest for the propagation of a disturbance in the SSTA field, evidenced by SPF1.

Let us now enter into the detail of how the zones were defined. As already said, the spatial pattern of AMC1 presents a number of local maxima, visible in Fig. 1; the highest in ECEPO, the second in NTIO etc.. Recall moreover, from Subsection 4.1.1, that Fig. 2 shows, multiplied by 100., the values of AMC1 exceeding 0.3; Fig. 3 shows instead AMC1 values exceeding 0.6, also multiplied by 100..

On the basis of values exceeding 0.4, the nine zones were formed, each one containing at least a local AMC1 maximum >0.5 (zones n. 1,2,4,5,6,7), or deriving from the fragmentation of a bigger ensemble, but still having inside at least one value >0.5 (zones n. 3,8,9).

At this point, a base j (e.g. the absolute ECEPO maximum) was cross-correlated, at lag τ, with all the grid points included in the various zones; at last, the values of cross-correlation obtained, exceeding the usual threshold 0.3, were averaged over the points belonging to a given zone. Be $C_a(j, jz, \tau)$ the average cross-correlation at lag τ between the base j and the stations included in the jz-th zone; be $C_e(j, jz, \tau)$ the extremal value (positive or negative, that is, maximum or minimum) of cross-correlation at lag τ between the base j and the stations included in the same zone. By looking, for a fixed base, at the way the plots of C_a versus τ (as well as those of C_e versus τ) change when one moves from one zone, jz, to the other, will, as we shall see, help recognizing the information about lead-lag relations in the data.

The whole procedure was based on AMC1 values (for the choice of the zones) because, on the one hand, the first mode is the one that explains the highest percentage of total variance; on the other hand, because it is the one that proved to be most connected with ENSO phenomena and to be peculiar of intertropical oceans; at last, it was the only one assuming significant amplitude values over the area possibly interested by the propagation of disturbances from the Pacific to Indian, that is over the longitude belt 100°–125°E.

6. Correlation analysis results

6.1 *Correlation among original SSTA series*

The correlation analysis described above was performed, with original data, taking two different base stations, the one in ECEPO and the one in NTIO; moreover, for each base it was repeated twice: first, by computing cross-correlations on the basis of all data available; then, by considering only El Niño periods (see Table 1). Here, however, only the results concerning all 40 years will be presented, since those relative to only El Niño periods turned out to be quite noisy, due to poor statistics (133 time steps instead of 480).

The $C(\tau)$ functions were, for each base, computed for values of τ from −12 months to +12 months.

Figs. 13a and 13b show examples of the curves of $C_a(\tau)$ and $C_e(\tau)$ that were obtained, with the procedure described in Section 5, from the fields of $C(\tau)$; in particular, the figures concern the AMC1 maximum located in ECEPO, taken as a base (the zone containing the base is zone n.1, shown in Fig. 2). All zones show, if any, a positive correlation with ECEPO base.

The majority of the curves are quite flat (flatter, of course, for average values than for extremal values), and therefore it is not easy to recognize at which lag the base and a given zone are best correlated. The only zones for which a kind of bell-shaped curve emerges (apart from zone n.1 itself, that, obviously, gives a peak at $\tau=0$, with 1. as the peak value for $C_e(\tau)$) are the neighbours of zone n.1 (see Fig. 2), namely, zone n.2 (eastwards) and zone n.3 (westwards). However, in both cases the "bell" is fairly symmetrical and centered on values of lag

close to zero.

The only "message" that can be extracted from these figures consists in the range of lag values over which the correlation exceeds the threshold value 0.3 (and therefore appears, as an asterisk or a cross, in Figs. 13a and b). Following this idea it may be noticed that negative lags (leads) of about 1 month of zone n.2 with respect to base-zone n.1 seem favoured, while for zone n.3 positive lags (delays) seem to be slightly favoured (the range of τ values is [−7,+10 months]); however, the message is not confirmed by zone n.4 [−7,+7 months]. This result seems to give some evidence of a westward shift of the SSTA signal from zone n.2 to zone n.3.

Zone n. 5 (NIO) definitely seems to favour positive lags [−6,+12 months] of NTIO with respect to ECEPO: this confirms that information should actually travel from Pacific to Indian Ocean and not vice-versa. The neighbouring zone n.9 (SSC, not shown) strengthens this impression: the τ range is [−3,10 months].

In the Atlantic, the correlation extends over [0,+8 months] for zone n. 8. If any, the message is "the SSTA information travels from ECEPO to the Atlantic Ocean".

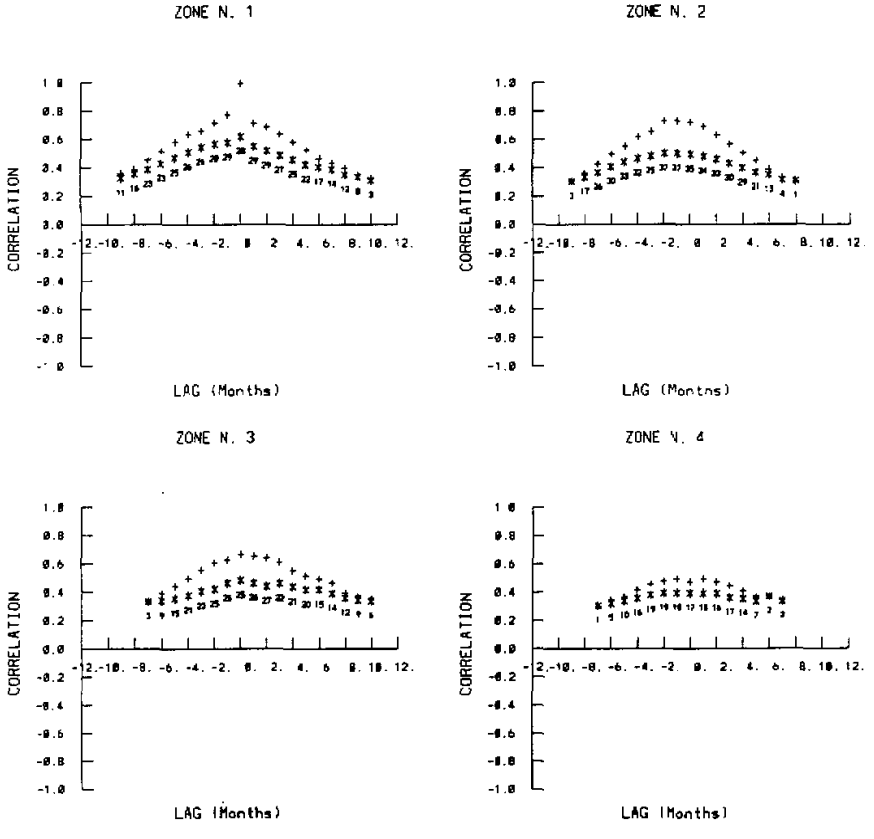

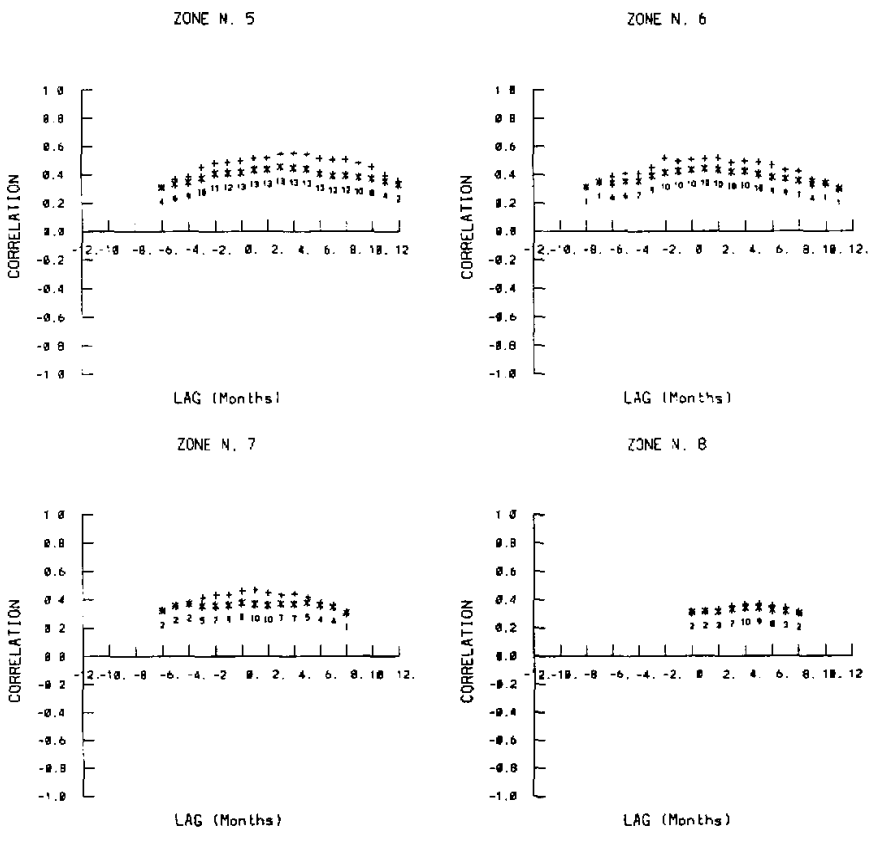

Fig. 13. Values of $C_a(\tau)$ (*) and $C_e(\tau)$ (+) for the various zones. The values are relative to the point correlation analysis performed on the original SSTA field, as described in Section 6. $C_a(\tau)$ is, at lag τ, the average correlation between the base station, that in this case is the maximum of AMC1 located in ECEPO, and the stations included in each zone; only correlation values exceeding the threshold 0.3 were taken into account when computing the average. $C_e(\tau)$ is the corresponding extremal correlation found inside the zone. The small numbers appearing in the figures, close to the * symbols, represent the number of grid points of the zone, contributing to the $C_a(\tau)$ value illustrated. The zone containing the base is n.1. (a) Zones n.1–4; (b) zones n.5–8.

Limiting the attention to the intertropical belt, in an attempt to summarize, we may list the central abscissa of the distributions found for zones n.3 and 4 (Pacific, westward of n.1), n.2 (Pacific, eastward of n.1), n.6,5,9 (NTIO and neighbours) and n. 8 (Atlantic), when the base is in zone n.1. Excluding values of τ at which less than three stations contribute to the average value shown in Figs. 13a and b, we find: +1.5 (zone n.3), 0. (zone n.4); −1. (zone n.2); +1.5 months (zone n.6), +2.5 months (zone n. 5), +4. months (zone n. 9); +4.5 months (zone n.8). Zone n. 6 surprisingly seems to be less "delayed" than NTIO and SSC.

The analogous figures concerning the base in NTIO (zone n.5), not shown, confirm previous conclusion. When the base is in the Indian Ocean, the curves for zones n. 4,3,1,2 are flat but the τ ranges are [−11,2], [−12,6], [−12,6] and [−12,4 months]: a lead relation of the equatorial Pacific Ocean with respect to NTIO, centered on about −3 or −4 months, is thus favoured, as expected from previous discussion. The curve for zone n.6 is over [−12,11 months] and seems slightly asymmetrical, with negative lags favoured (the same rather puzzling hint found before, see the case of ECEPO base). For zone n. 9 the distribution is centered on −2 months (it extends over the range [−10, 6 months]), a fact that on one hand would perhaps suggest that the signal from ECEPO reaches SSC first and NTIO later; however, on the other hand, the curve is asymmetric and small positive lags seem to correspond to the highest correlation values, so the question remains open.

6.2 *Correlation among reconstructed series*

In an attempt to reduce the noise background, the entire computation for the two bases was repeated with data reconstructed on the basis of one or more c.p.c. modes, according to the formula given at the end of Section 3.

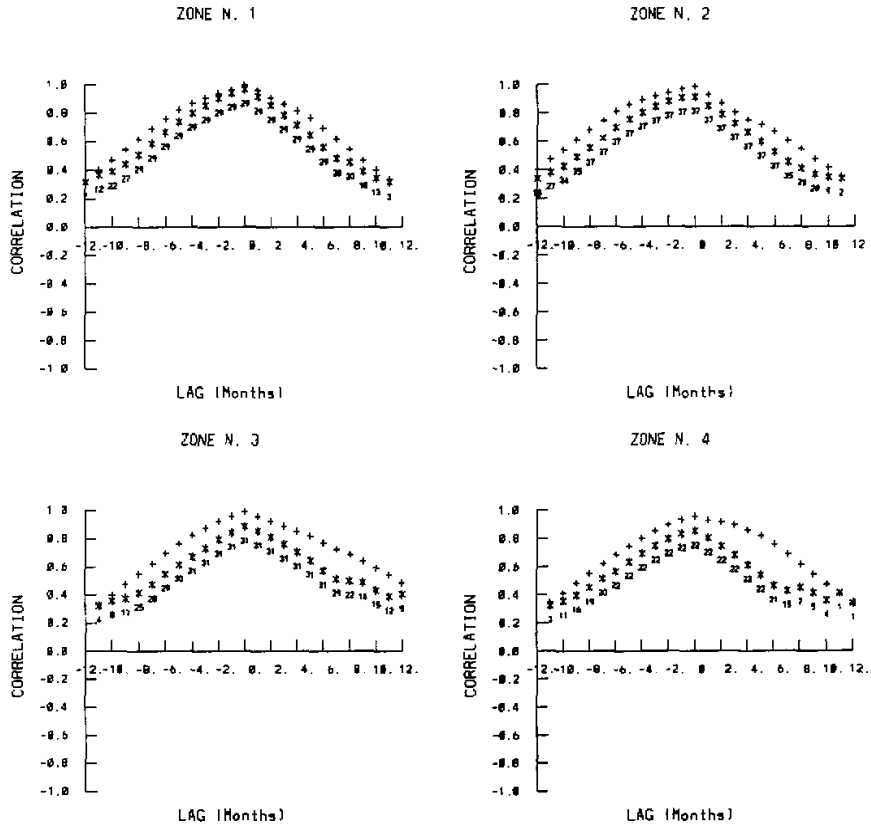

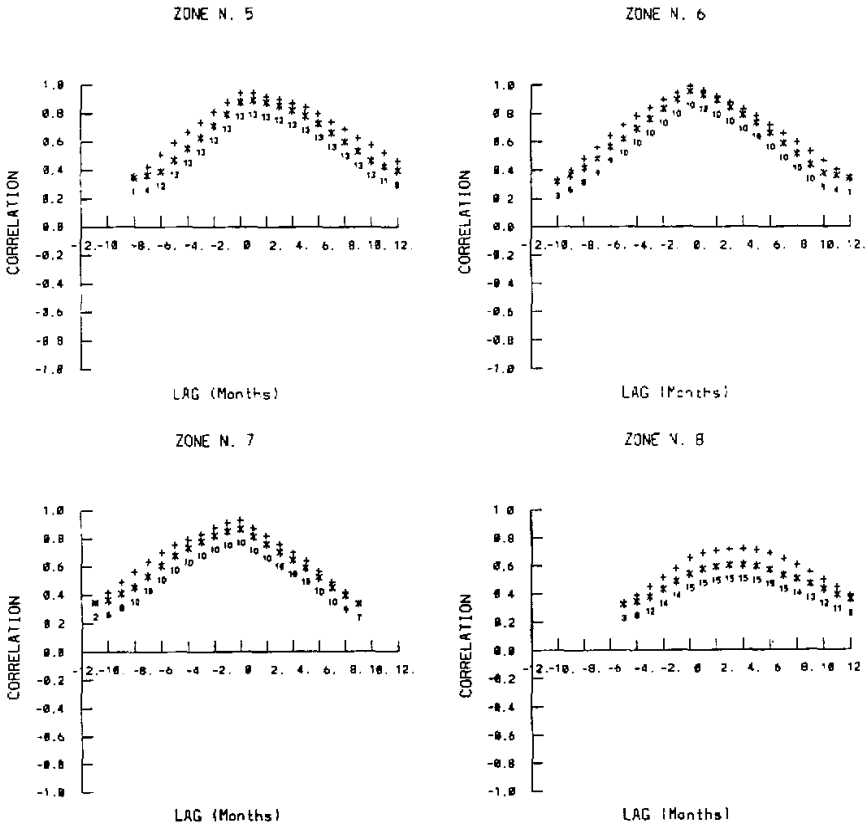

Fig. 14. (a) The same as Fig. 13 but relative to the point correlation analysis performed on the smoothed SSTA field, reconstructed on the basis of the first three c.p.c. modes. (a) Zones n.1–4; (b) zones n.5–8.

Only the curves of $C_a(\tau)$ and $C_e(\tau)$ that were obtained, for the ECEPO base, using data reconstructed on the basis of the first three modes are discussed here: they appear in Figs. 14a and b. It may be seen that in comparison with Figs. 13a and b, maximum and mean values (crosses and stars) are now closer to one another for a given value of τ, what, of course, means a more uniform behaviour inside each zone.

All zones are well correlated with ECEPO base: the correlation is positive for all zones. *Zone n.9 (not shown) is positively correlated with ECEPO at lags greater than −6 months and* negatively correlated for greater leads. This is not in disagreement with the case of original data, since in that case a positive correlation was found down to a 3 months lead.

It is clearly visible from Figs. 14a and b that the clue in favour of a propagation from the Pacific to the Indian Ocean now emerges much better than with original data (Section 6.1). For example, the curve for zone n.5 is now well asymmetric; the skewness of the curve clearly evidences that delay that was instead less visible for original data. The trend for zone n. 9 (not included in the figures) turns out to be even clearer than for n.5: as already mentioned, at ex-

treme lead values zone n.9 becomes even anti-correlated with the base and the whole curve is quite asymmetric. The peak of the $C_a(\tau)$ curve is around a +(3–4) months lag.

Zone n.2, close to the coast of South America, leads zone n. 1, as seen for original data in Subsection 6.1; also zone n. 7 (Californa coast) gives the same suggestion. Zones n. 3 and 4 have more symmetrical curves.

As for the Atlantic, zone n. 8 favours again positive lags: besides the asymmetry, the bell-shaped curve is centered on a 3–4 months lag value.

For the case of NTIO base, similar results are found.

It may be worthwhile noting that if one repeats the analysis with data reconstructed on the basis of the first mode only, one obtains results very close to those obtained with the first three modes together (the corresponding figures are not shown). This fact once more supports the idea that the key information concerning ENSO phenomena (and therefore the intertropical wave propagation) is contained in the first complex mode.

7. Conclusion

A complex principal component (c.p.c.) analysis was carried out on 40 years of SST monthly averages of the Pacific, Indian and Atlantic Oceans, in the attempt to reveal the main space and time structures of stationary and travelling thermal disturbances.

As the regions of highest AMCI values were found in the south eastern tropical Pacific and in the north tropical Indian Oceans, where the onset of the warm phase of the Southern Oscillation coincides with the warm phase of the seasonal cycle (Philander, 1990), and as their space phase turned out to be the same, the first complex eigenmode of the SSTA field singled out this particular behaviour of El Niño and can be called as El Niño pattern.

The westward travelling features appearing in the Pacific Ocean provide some evidence of reflected Rossby waves, representing the west phase of the signals that propagate disturbances of thermal structure in the tropical Pacific Ocean.

The fact that the equatorially trapped Kelvin wave, that is expected to bring the warming signal from the warming pool toward the eastern boundary of the Pacific Basin, is not seen in this analysis of sea surface temperature data, is in agreement with recent findings (TOPEX experiment), revealing that this rôle is played by underwater Kelvin oscillations, not appearing as temperature anomalies at the surface.

One of the authors (S. Alessio) would like to thank Prof. Wang Bikui of the University of Science and Technology of China (Hefei, P.R. China) for her useful advice and comments.

This research has been carried out in the frame of the World Laboratory Project LAND-2 (Drought and Desertification) and with the support of the TRIL Programme sponsored by ICTP - Trieste (Italy).

REFERENCES

Barnett, T. P., 1983: Interaction of the monsoon and Pacific trade wind system at interannual time scales, Part I: The equatorial zone. *Mon. Wea. Rev.*, **111**, 756–773.

Clarke A. J., and A. Lebedev, 1996: Long term change in the equatorial Pacific trade winds. *J. Climate*, **9**, 1020–1102.

Fu Congbin, Quan Xiaowei, and Su Bingkai, 1988: Study on the amplitude and phase variation of equatorial warming by using complex EOF (CEOF) analysis. *Kexue Tongbao (Chinese Science Bulletin)*, **33(N. 20)**, 1718–1722.

Horel, J. D., 1984: Complex principal component analysis: theory and examples. *J. Climate Appl. Meteor.*, **23**, 1660–1673.

Longhetto A., and Wang Bikui, 1993: Combined principal component and complex principal component analysis of SST anomalies over Pacific Ocean in connection with El Niño recurrence periods. *Chinese Journal of Atmospheric Sciences*, **17(2)**, 105–113.

Lough J. M., 1986: Tropical Atlantic sea surface temperatures and rainfall variations in sub-Saharian Africa. *Mon. Wea. Rev.*, **114**, 561-570.

Philander, S. G. H., 1990: *El Niño, La Niña and the southern oscillation*. Academic Press, U.S.A. 33 pp.

Shi Jiuen, 1990: ENSO and anti-ENSO episodes in recent 40 years and the northwest Pacific typhoon activity, Paper presented at the *International TOGA Scientific Conference*, Honolulu, Hawaii.

Zhang Y., J. M. Wallace, and D. S. Battisti, 1997: ENSO-like interdecadal variability: 1900-1993. *J. Climate*, **10**, 1004-1020.